Uranus's northern polar cap in 2014

Daniel Toledo[1], Patrick G. J. Irwin[1], Nicholas A. Teanby[2], Amy A. Simon[3], Michael H. Wong[4] and Glenn S. Orton[5]

[1]Department of Physics (Atmospheric, Oceanic and Planetary Physics), University of Oxford, Parks Rd, Oxford OX1 3PU, UK.

[2]School of Earth Sciences, University of Bristol, Wills Memorial Building, Queens Road, Bristol, BS8 1RJ, UK.

[3]NASA Goddard Space Flight Center Solar System Exploration Division (690) Greenbelt, MD 20771, USA.

[4]Astronomy Department, University of California, Berkeley CA 94720-3411, USA

[5]Jet Propulsion Laboratory, California Institute of Technology, 4800 Oak Grove Drive, Pasadena, CA 91109, USA.

Corresponding author: Daniel Toledo (daniel.toledocarrasco@physics.ox.ac.uk)

Key Points:

- Aerosols, dynamics, Equinox

Abstract

In October and November 2014, spectra covering the 1.436 – 1.863-μm wavelength range from the SINFONI Integral Field Unit Spectrometer on the Very Large Telescope showed the presence of a vast bright North polar cap on Uranus, extending northward from about 40ºN and at all longitudes observed. The feature, first detected in August 2014 from Keck telescope images, has a morphology very similar to the southern polar cap that was seen to fade before the 2007 equinox. At strong methane-absorbing wavelengths (for which only the high troposphere or stratosphere is sampled) the feature is not visible, indicating that it is not a stratospheric phenomenon. We show that the observed northern bright polar cap results mainly from a decrease in the tropospheric methane mixing ratio, rather than from a possible latitudinal variation of the optical properties or abundance of aerosol, implying an increase in polar downwelling near the tropopause level.

1 Background

Uranus undergoes a cycle of dramatic seasonal atmospheric changes in cloud and hazes, driven by its extremely large obliquity (98º). Different observations have revealed, for instance, the presence of discrete clouds and convective systems at different locations and time periods (e.g. Irwin et al., 2017; de Pater et al., 2015; Sromovsky & Fry, 2007), or the formation and dissipation of bright polar regions in both hemispheres before and after the 2007 equinox (e.g. Hofstadter & Butler, 2003; Irwin et al., 2016; Irwin, Teanby, et al., 2012; Karkoschka, 2001; Karkoschka & Tomasko, 2009; Rages et al., 2004; Sromovsky & Fry, 2007). Voyager observations of Uranus in 1986 recorded for the first time the presence of a bright south polar cap extending southward from about 45ºS. Although observations made between 1994-2003 showed temporal variations in brightness in the south polar region, they did not record signs of a northern polar cap with comparable brightness to that observed in the south pole (Hammel & Lockwood, 2007; Rages et al., 2004). Near equinox in 2007, however, Uranus' atmosphere underwent a number of seasonal changes that led to a reversal in the polar brightness: a south polar collar at 45ºS diminishing in brightness relative to mid-latitudes, and a north polar collar at 45ºN becoming steadily brighter with time (Irwin, Teanby, et al., 2012). In August 2014, a large bright polar-cap-like feature was identified in Uranus's northern pole from Keck telescope images (de Pater et al., 2015), whose progressive formation over 2013 was observed by amateur telescopes (see PVOL database, Hueso et al., 2018). Based on long-term records of Uranus brightness variations before the 2007 equinox (Hammel & Lockwood, 2007; Lockwood & Jerzykiewicz, 2006), it was thought that the polar cap could be a seasonal formation or re-distribution of aerosols (de Pater et al., 2015; Sromovsky et al., 2015).

Observations of Uranus in October and November 2014 with the Wide Field Camera 3 (WFC3) instrument of the Hubble Space Telescope (HST) and the SINFONI Integral Field Unit Spectrometer on the Very Large Telescope (VLT) confirmed the presence of the ubiquitous bright cap from 40º to 90ºN (**Figure 1a**) (Irwin et al., 2017). The feature does not appear at 1.47 and 0.727-μm methane-absorbing wavelengths, where the fraction of radiance transmitted to space is less than 0.5 for pressures greater than ~ 0.1 bar, the pressure of the tropopause. This indicates that if the polar cap is the result of variations in aerosol distribution, these variations must occur at altitudes below the tropopause. This result was also tested using the cloud properties and methane concentration obtained at polar cap latitudes (see section 3.2). The purpose of this work is to determine the nature of Uranus's polar cap in 2014. To this end, we analyzed spectra covering the

1.46-1.70-μm wavelength range of the VLT/SINFONI observations taken in 2014, which provide a clear mapping of the feature at both high spatial and spectral resolution.

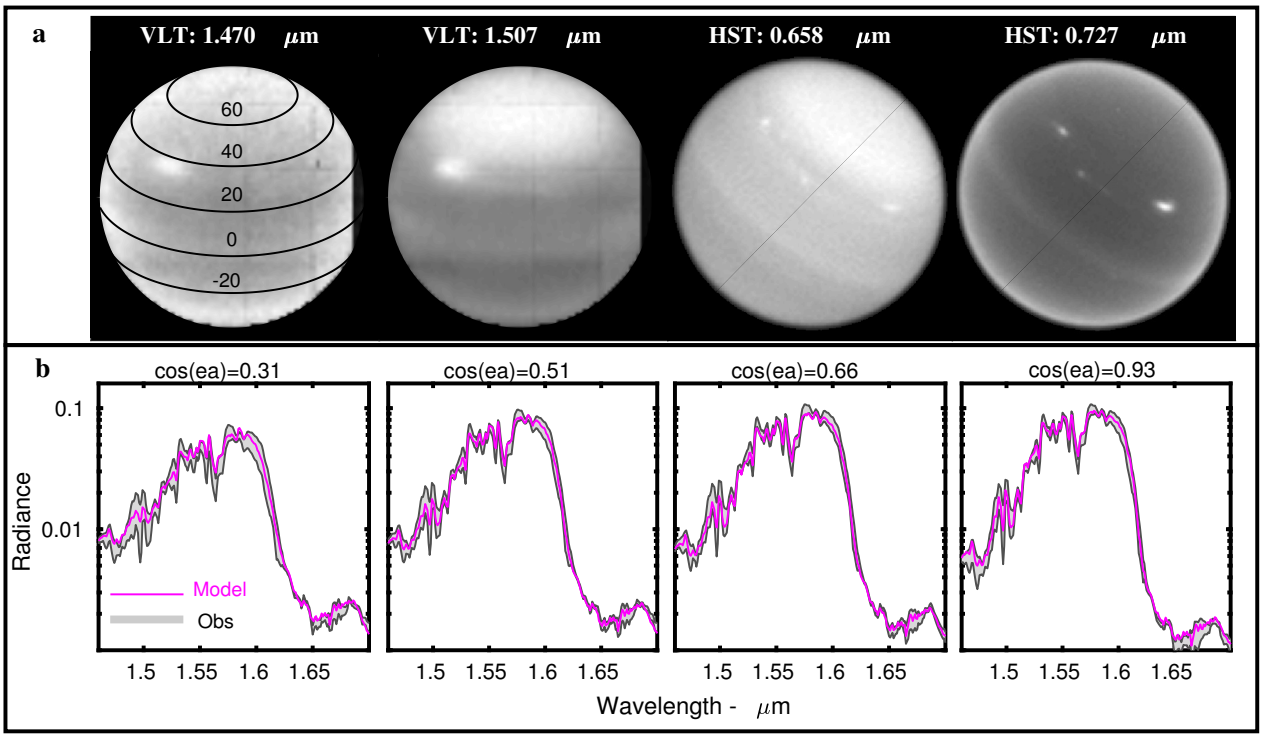

Figure 1. (a) VLT and HST images at 1.470, 1.507, 0.658 and 0.727 μm made on 31st October and 9th November 2014, respectively. The polar cap can be identified at 1.507 and 0.658 μm for latitudes higher than 40ºN. (b) Comparisons between radiative-transfer model and observations at 32ºN. The thick grey solid lines represents VLT spectra with errors at 32ºN (far away from the polar cap) with emission angles (ea) of 72º, 59º, 49º and 22º respectively (cos(ea)=0.31, 0.51, 0.66 and 0.93). These observations were selected at longitudes away from the storm system observed in VLT and HST images (Irwin et al., 2016; Irwin et al., 2017). The shaded errors represent the random errors of the observed radiances and are computed by the VLT/SINFONI pipeline. The four spectra were fitted simultaneously using the 3-cloud model discussed in section 3 (purple dashed lines) whose reduced chi-squared value was found to be 0.77.

2 Observations, cloud model and radiative transfer analysis

We analyzed observations of Uranus performed by the SINFONI instrument on October 31st and November 11th, 2014, at the European Southern Observatory (ESO) Very Large Telescope (VLT) in Paranal, Chile. SINFONI is an Integral Field spectrograph that can make use of adaptive optics to yield a spatial resolution of about 0.1" and returns 64×64-pixel spectral cubes, where each "spaxel" has 2048 wavelengths. SINFONI has three spaxel scale settings: 0.25", 0.1" and 0.025" resulting in fields of views (FOV) of 8" × 8", 3" × 3" and 0.8" × 0.8", respectively. Uranus was imaged with the 0.1" pixel scale and the H-grism, which has a spectral resolution of 0.0005 μm and covers the wavelength range 1.436 – 1.863 μm. The data were first reduced with the ESO VLT SINFONI pipeline, with additional photometric corrections as described by Irwin et al.

(2016), and then averaged with a triangular-shaped instrument function with Full Width Half Maximum (FWHM) = 0.002 μm, resulting in a final spectral resolution of R ~ 775. It was found in previous analyses of Uranus that this spectral resolution provides the best compromise between modelling computational speed, signal-to-noise (SNR) ratio and accurate representation of the methane absorption features (Irwin, de Bergh, et al., 2012).

The NEMESIS correlated-k radiative-transfer and retrieval code (Irwin et al., 2008) was used to simulate the absorption and scattering of Uranus's atmosphere. The methane absorption was calculated using the WKMC-80K line database (Campargue et al., 2012) and assuming the 'F1' temperature profile of Sromovsky et al., (2011) which has a He:H_2 ratio of 0.131 and assumes a 0.04% mole fraction of neon and a deep CH_4 mole fraction of 4% at non-polar latitudes (Karkoschka & Tomasko, 2009). Although the temperature profile may change at polar latitudes, these changes are not expected to cause an impact in our retrievals since the thermal structure of Uranus is not strongly variable. We tested what is the effect of adding a random noise with different amplitudes to the F1 profile, and we found that the retrieved aerosol parameters do not differ significantly. Figure S1 in the supporting information provides more detail on these tests. The line data were converted to k-distribution look-up tables, covering the VLT spectral range and assuming a triangular-shaped instrument function with FWHM = 0.002 μm. Collision induced absorptions by H2–H2 and H2–He collision-induced (CIA) were computed using the coefficients of Borysow et al. (1989), Borysow et al. (2000), and Zheng & Borysow (1995) and an equilibrium ortho/para-H2 ratio was assumed at all altitudes and locations. Absorption by H2–CH4 and CH4–CH4 collision-induced was also computed (Borysow & Frommhold, 1987). Although the assumption of equilibrium ortho/para-H2 may not valid for all the latitudes, we emphasize that for our wavelength range this parameter does not have an impact on the retrievals.

3 Analysis procedure and results

3.1 Analysis at latitudes < 40ºN

To determine the nature of the polar cap, we first conducted a number of limb-darkening analyses of the VLT/SINFONI spectra (covering the 1.46-1.70-μm wavelength range) at latitudes away from the polar cap. For each latitude selected, four spectra taken at different emission angles (ranging from 20º to 75º) were fitted simultaneously using a three-layer cloud model comprising a thick tropospheric cloud based near the 2-bar pressure level and two vertically extended haze layers with bases in the troposphere (~ 0.56 bar) and near the tropopause (~ 0.19 bar); the first two pressure levels were selected based on previous analyses of clouds and haze (Irwin et al., 2016; Irwin et al., 2017; Sromovsky et al., 2011). The main difference of this model compared with the two-layer cloud model used in previous analyses (Irwin et al., 2016; Irwin et al., 2015; Irwin et al., 2017) is the addition of a stratospheric haze layer, which was required for fitting VLT spectra observed over a wide range of emission angles simultaneously. The vertical distribution of each cloud layer is characterized by the total opacity at 1.4 μm (τ), the fractional scale height (FSH) and the cloud base altitude (h), parameters that can be retrieved or kept fixed in the analysis. The aerosol scattering properties (single-scattering albedo, phase function and extinction cross-section) are computed at all wavelengths using Mie theory, with the phase functions approximated with Henyey-Greenstein functions to average over the characteristic 'glory' and 'rainbow' of spherical particles. To calculate these properties, the parameters required (that can be retrieved or kept fixed) are the size distribution of the aerosol particles, the imaginary refractive index spectrum (assumed

to be the same at all vertical levels), and the real part of the refractive index at a single wavelength; the real part of the refractive index at all other wavelengths is calculated using the Kramers-Kronig relation (e.g. Sheik-Bahae 2015).

The bases of the three layers were fixed in the model, while the fractional scale height was retrieved for the two haze layers, but fixed for the tropospheric cloud to a value of 0.01 (Irwin et al., 2016), to make it vertically thin. For the radiative-transfer simulations, the atmosphere was split into 39 levels equally spaced in log pressure between 12 bar and 0.003 bar. The total opacity, particle effective radius (assuming a standard Gamma distribution) and the imaginary part of the refractive index spectrum of each of the three cloud layers were retrieved. The real refractive index spectrum was derived using the Kramers-Kronig analysis assuming a real refractive index of 1.4 at a wavelength of 1.6 μm, and the spectrum of the imaginary refractive index was retrieved at 6 wavelengths assuming a certain correlation in order to retrieve a smooth spectrum (and so to avoid unrealistic variations). We find that effective radii of ~1 μm for the tropospheric cloud, and of ~ 0.8 and 0.05 μm, respectively, for the tropospheric and stratospheric haze layers provide the best results in the limb-darkening analyses performed at different non-polar latitudes. This model was able to achieve fits with reduced chi-squared (χ^2_{red}) values smaller than 1. **Figure 1b** shows, as an example, a limb darkening analysis carried out at 32ºN with the three-cloud model and whose retrieved refractive index is illustrated in **Figure 2**. Similar limb-darkening analyses performed at different latitudes showed that the imaginary refractive index spectrum (and derived real part) and size distribution of each cloud layer are very similar at all the locations. Therefore, for the analysis of the cloud and haze at polar latitudes we use the refractive index and size distribution derived in this section as reference.

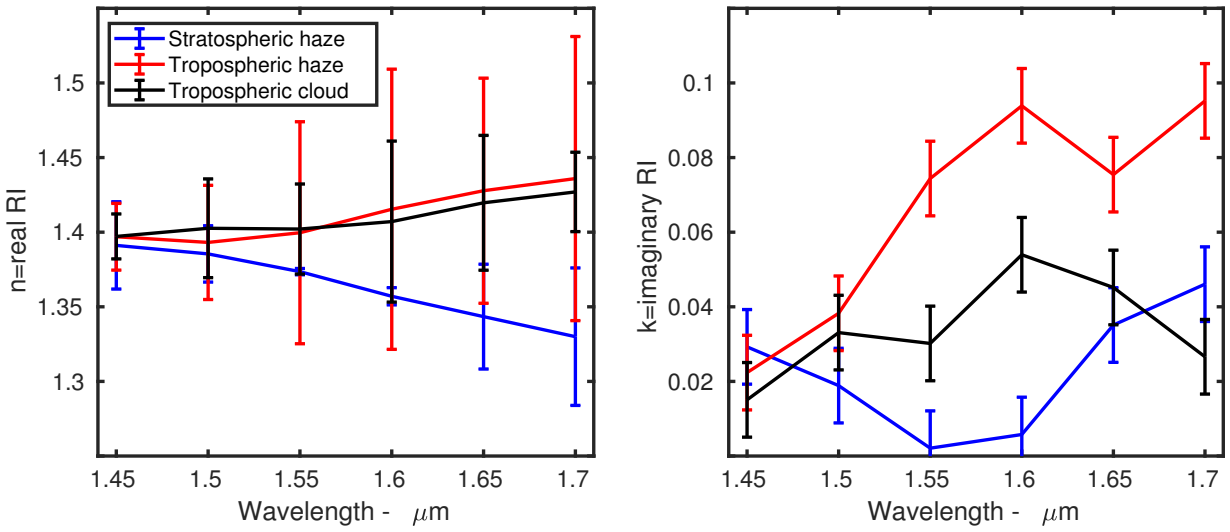

Figure 2. Fitted refractive index (RI) spectra from the limb-darkening observations using NEMESIS for the three cloud layers. Left panel shows the real RI and right panel the imaginary RI. Data at 32°N (outside the polar region) were used to constrain RI, but results for other latitudes were highly consistent with these values.

3.2 Analysis at polar-cap latitudes

The same 3-cloud model was used at latitudes lying within the polar 'cap', but assuming different values of the deep methane mixing ratio: 1.5, 2, 2.5, 3, 3.5 and 4%. This selection of

values is based on previous analyses that found a depletion of methane at polar latitudes (Irwin, Teanby, et al., 2012; Karkoschka & Tomasko, 2009; de Kleer et al., 2015; Sromovsky et al., 2011, 2014; Tice et al., 2013). For different polar latitudes, we fitted four spectra taken at different emission angles (whose range of values depends on the latitude) for these different methane concentrations and using the refractive index and size distribution derived in previous section (latitudes <40ºN). Although this 3-cloud model is able to achieve fits with χ^2_{red} values <1 at polar latitudes, we found a strong correlation between the tropospheric cloud altitude and the methane concentration. This correlation results from the fact that the absorption of light by methane above the cloud deck is reduced as the cloud altitude increases. Therefore, an overestimation of the deep methane volume mixing ratio (CH_4 VMR) in the pole can occur if the retrieved tropospheric cloud altitude (h_{tc}) is higher at these latitudes. In order to study the possible combinations of solutions we carried out a number of limb-darkening analyses for a set of cloud altitudes (-24, -22, -20, -18, -16, -14 and -12 km, or in pressure units 2, 1.89, 1.78, 1.68, 1.58, 1.47 and 1.22 bars, respectively) and deep methane volume mixing ratios (0.015, 0.020, 0.025, 0.030, 0.035 and 0.040). For each h_{tc}-CH_4 VMR combination, we retrieved the opacity of the three cloud layers and the FSH of the two haze layers by fitting four spectra taken at different emission angles. These limb-darkening analyses were conducted at latitudes within and near the polar cap edge. The upper panels of **Figure 3** show contour plots of χ^2_{red} in the h_{tc}-CH_4 VMR space for limb-darkening analyses performed at 38º, 42º, 55º and 70ºN, while the lower panels show the contour plots of the retrieved tropospheric cloud opacity (τ_{tc}). Note that limb-darkening analyses at higher latitudes were not performed due to the limited range of emission angles at such latitudes. For example the emission angles of the observations at 38ºN were found to lie between 17º-73º while at 70 ºN between 43º-73º. We tested that this change in the emission-angle range between the different latitudes does not have a major impact on our retrievals (see figure S2 in the supporting information for more details).

We observe that at 38º and 42ºN (far-from and near-to the polar cap edge) the minimum values of χ^2_{red} are found for CH_4 VMRs greater than 0.03, while at 55º and 70ºN (within the polar cap) the best solutions are given for values between 0.02 and 0.04. Sromovsky et al., (2014) found CH_4 concentrations smaller than 0.03 at latitudes polewards of 40ºN and of ~ 0.035-0.04 for the rest of non-polar latitudes in 2012, using wavelength ranges with complementary hydrogen and methane absorption. Assuming a similar distribution of methane in 2014, the lower panels of **Figure 3** show a retrieved opacity at 1.4 μm of the tropospheric cloud of 2.5 ± 0.4 at 38ºN and 2.8±0.4 at 70ºN. In order to examine the main polar cap signatures in the VLT spectra and to study whether such an increase in the tropospheric cloud opacity can cause the change in brightness seen in both VLT and HST images (see **Figure 1a**), we took the difference between spectra at the 26º and 46ºN locations (**Figure 4a**). These signatures can be compared with those observed when changing some of the parameters of the model, such as the tropospheric cloud opacity or the CH_4 VMR. We found that the polar cap signature illustrated in **Figure 4a** does not correlate well with the variation obtained in the simulated 46ºN spectrum when the tropospheric cloud opacity is increased from 2.5 to 3 or from 2.5 to 3.5. Note also that results illustrated in **Figure 3** show tropospheric cloud opacity differences between polar and non-polar latitudes of only ~0.5 (close to our formal uncertainty $\Delta\tau_{tc}$=0.4). Therefore, these results indicate that the mean features of the polar cap are not the result of a significant variation of the tropospheric cloud opacity. Similar conclusions are derived for the tropospheric haze for which we found opacities of 0.049±0.001 and 0.0395±0.0015 at 38 and 70ºN, respectively (i.e. a slight decrease in the polar latitudes). Regarding the stratospheric haze, we found opacities of 0.242±0.003 and 0.263±0.004 at 38 and 70ºN,

207 respectively. This 10% increase in stratospheric haze opacity near the pole is a statistically
208 significant difference, but it cannot be the cause of the prominent polar cap because the polar
209 brightening is seen only at wavelengths probing deeper than the tropopause (Sec. 1).
210 These results show that the polar cap observed in VLT images cannot be explained by an
211 accumulation of aerosol; neither by variations in the cloud/haze scattering properties since the
212 same refractive indices and size distributions derived in section 3.1 at 32°N were used and found
213 to provide a good fit. The observed timescales for the formation of the polar cap discards a possible
214 haze accumulation due to changes in haze mass production rate over the solar cycle after 2007
215 equinox. Indeed, the response of the haze to changes in its production rate is much too sluggish
216 (Pollack et al., 1987) to explain the polar cap formation. Thus, this indicates that dynamics may
217 be important on the formation of the polar cap through variations in the atmospheric circulation
218 before and after 2007 equinox. These variations in the atmospheric circulation would lead to a
219 redistribution of the haze (particle size and column mass) by transporting small particles from
220 upwelling regions to the North pole. Although this transport of small haze particles to the polar
221 region could play a role in the polar cap formation, their small cross section at near-IR wavelengths
222 (small optical depth) may explain why our limb-darkening analyses do not show a noticeable
223 latitudinal variation in the aerosol properties.
224 Results illustrated in the upper panels of **Figure 3** show that the observations in the polar cap
225 and near the polar cap edge (determined by the change in brightness in VLT and HST images) can
226 be fitted using a lower CH_4 concentration and a similar tropospheric cloud altitude to that found at
227 non-polar latitudes. We found also that the polar cap signature illustrated in **Figure 4a** correlates
228 well with the variation obtained in the simulated 46ºN spectrum when the methane mixing ratio is
229 modified from 4 to 2% or from 4 to 3% (**Figure 4b**). Since these mixing ratios correspond to the
230 values found at latitudes outside and within the polar 'cap', the results shown in **Figures 4b** suggest
231 that the strong contrast observed between the polar 'cap' and lower latitudes is mainly the result
232 of the depletion of methane. Note that at polar latitudes methane mixing ratios between 2 and 4%
233 (**Figure 3**) can provide good fits because the altitude of the tropospheric cloud is a free parameter
234 as well. Since the absorption of light by methane increases as the cloud altitude decreases, similar
235 signatures as illustrated in **Figures 4b** can be produced by increasing the cloud altitude in the
236 model. However, the possibility of an increase of the brightness as a result of an increase in the
237 cloud altitude (instead of from a decrease in the methane mixing ratio) is not consistent with the
238 observed tropospheric methane depletion at pressure levels not greater than ~ 3 bar at polar
239 latitudes (Sromovsky et al., 2014).
240

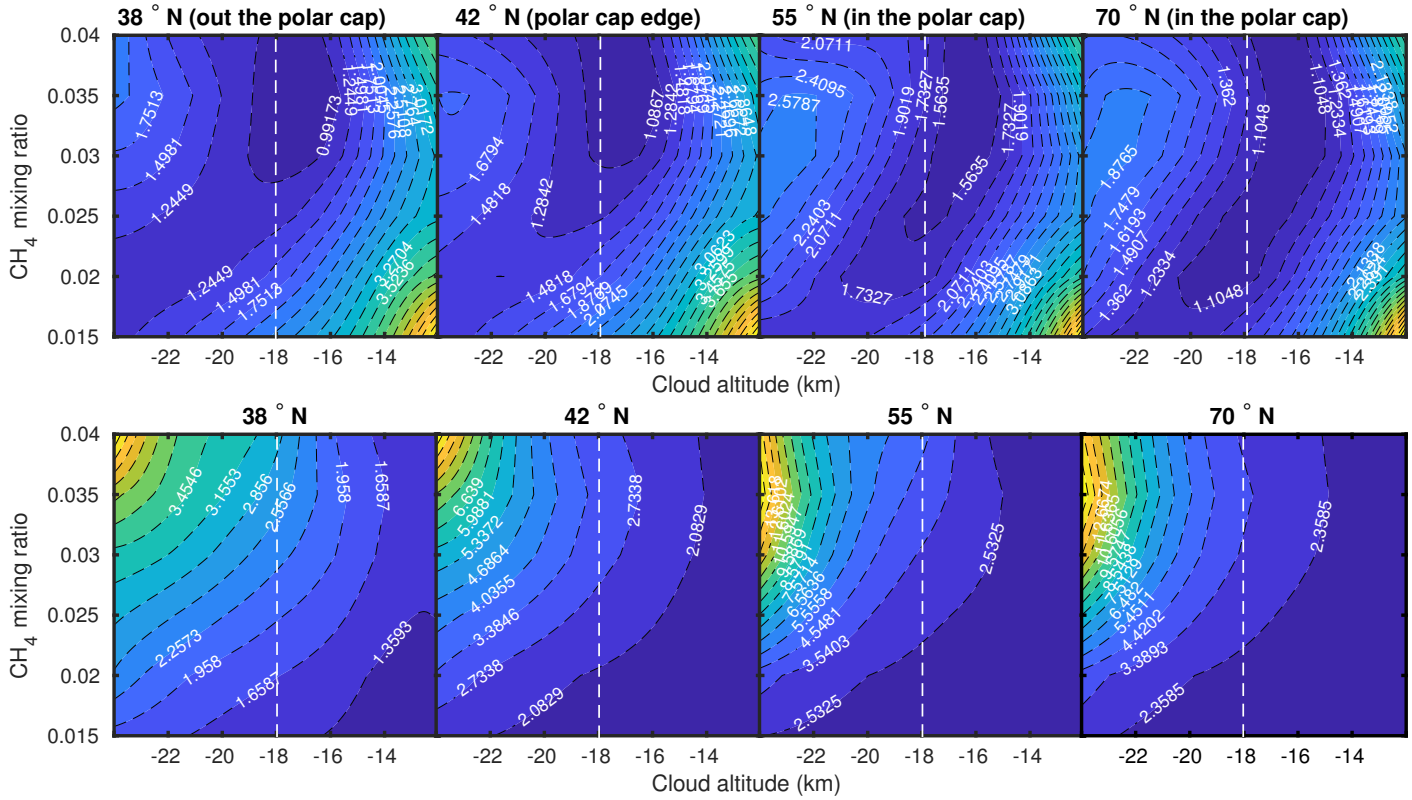

Figure 3. Contours of χ^2_{red} (upper panels) in the h_{tc}-CH_4 VMR space obtained from a number of limb-darkening analyses performed at 38º, 42º, 55º and 70ºN. Lower panels show contours of the tropospheric cloud opacity retrieved from these analyses. The altitudes -24, -22, -20, -18, -16, -14 and -12 km correspond to the pressure levels 2, 1.89, 1.78, 1.68, 1.58, 1.47 and 1.22 bar, respectively.

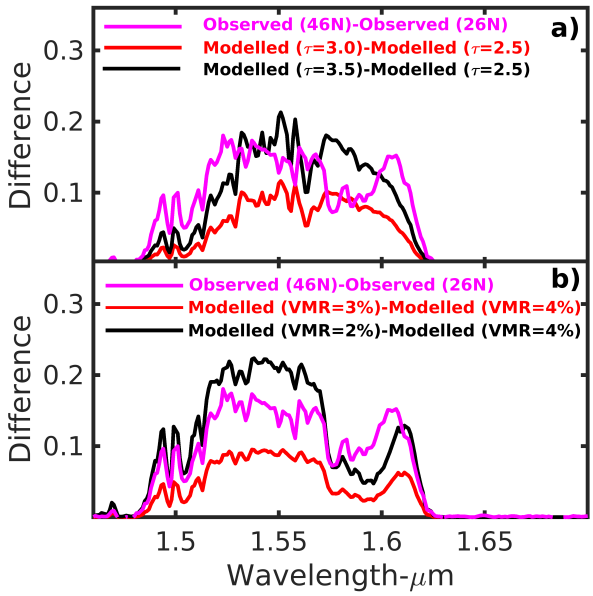

Figure 4. (a) Differences between observed spectra at 46º and 26ºN (ea~20º) showing the polar 'cap' spectral signature in the VLT spectra (purple solid line), and variations in the simulated 46ºN spectrum when the tropospheric cloud opacity is changed from 2.5 to 3 (red solid line) and from 2.5 to 3.5 (black solid line). (b) Differences between observed spectra at 46º and 26ºN (ea~20º) showing the polar 'cap' spectral signature in the VLT spectra (purple solid line), and variations in the simulated 46ºN spectrum when the CH_4 mixing ratio is changed from 4 to 3% (red solid line) and from 4 to 2% (black solid line). The comparison in panel b shows that the main polar cap spectral signature is similar to that obtained when the methane mixing ratio is varied from the value found at polar latitudes to that at latitudes far away from the feature.

4 Conclusions

The bright polar cap observed by VLT/SINFONI and HST/WFC3 in 2014 is mainly due to the decrease in the methane concentration at polar latitudes. By observing the brightness spatial variations, the VLT observations show the presence of the polar cap at latitudes 40º to 90ºN, indicating a hole-like depletion of methane. This methane latitudinal distribution supports scenarios consisting of an upwelling of methane gas at low latitudes, a condensation of methane in the cooler troposphere, and a descent of the now dried-out gas back to the deep atmosphere at high latitudes (Karkoschka & Tomasko, 2009; Sromovsky et al., 2011). The temporal variation of the latitudinal distribution of methane depletion can result from latitudinal variations in the gas upwelling rates, which in turn may be due to a Hadley overturning circulation or to a latitudinal variation in the rate of vertical eddy mixing. However, for clarifying which processes are involved in the formation and stability of the northern polar cap we require coupled dynamics-microphysics simulations of Uranus' atmosphere. These coupled simulations will clarify the role played by methane clouds in the polar methane depletion, and therefore in the polar cap formation.

Acknowledgments

The VLT/SINFONI observations were performed at the European Southern Observatory (ESO), Proposal 092.C-0187. The HST observations were made with the NASA/ESA Hubble Space Telescope under programs GO13937/14334. Support for this latter program was provided

by NASA through a grant from the Space Telescope Science Institute, which is operated by the Association of Universities for Research in Astronomy, Inc., under NASA contract NAS5-26555. Daniel Toledo, Patrick Irwin and Nicholas Teanby acknowledge the support of the UK Science and Technology Facilities Council. Glenn Orton acknowledges support from the National Aeronautics and Space Administration that were distributed to the Jet Propulsion Laboratory, California Institute of Technology. Telescope data are publicy available in ESO repository (http://archive.eso.org/eso/eso_archive_main.html).

References

Borysow, A., Borysow, J., & Fu, Y. (2000). Semi-empirical model of collision-induced absorption spectra of H2-H2 complexes in the second overtone band of hydrogen at temperatures from 50 to 500 K. Icarus, 145(2), 601–608. https://doi.org/10.1006/icar.2000.6384

Borysow, A., & Frommhold, L. (1987). Collision induced rototranslational absorption spectra of CH4–CH4 pairs at temperatures from 50 to 300 K. Astrophysical Journal, 318, 940–943.

Borysow, A., Frommhold, L., & Moraldi, M. (1989). Collision-induced infrared spectra of H2–He pairs involving 0–1 vibrational transitions and temperatures from 18 to 7000 K. The Astrophysical Journal, 336, 495–503.

Campargue, A., Wang, L., Mondelain, D., Kassi, S., Bézard, B., Lellouch, E., … Drossart, P. (2012). An empirical line list for methane in the 1.26-1.71μm region for planetary investigations (T=80-300K). Application to Titan. *Icarus*, *219*(1), 110–128. https://doi.org/10.1016/j.icarus.2012.02.015

Hammel, H. B., & Lockwood, G. W. (2007). Long-term atmospheric variability on Uranus and Neptune. *Icarus*, *186*(1), 291–301. https://doi.org/10.1016/j.icarus.2006.08.027

Hofstadter, M. D., & Butler, B. J. (2003). Seasonal change in the deep atmosphere of Uranus. *Icarus*, *165*(1), 168–180. https://doi.org/10.1016/S0019-1035(03)00174-X

Hueso, R., Juaristi, J., Legarreta, J., Sánchez-Lavega, A., Rojas, J. F., Erard, S., … Le Sidaner, P. (2018). The Planetary Virtual Observatory and Laboratory (PVOL) and its integration into the Virtual European Solar and Planetary Access (VESPA). Planetary and Space Science, 150, 22–35. https://doi.org/10.1016/j.pss.2017.03.014

Irwin, P. G. J., Tice, D. S., Fletcher, L. N., Barstow, J. K., Teanby, N. A., Orton, G. S., & Davis, G. R. (2015). Reanalysis of Uranus' cloud scattering properties from IRTF/SpeX observations using a self-consistent scattering cloud retrieval scheme. *Icarus*, *250*, 462–476. https://doi.org/10.1016/j.icarus.2014.12.020

Irwin, P. G. J., Fletcher, L. N., Read, P. L., Tice, D., de Pater, I., Orton, G. S., … Davis, G. R. (2016). Spectral analysis of Uranus' 2014 bright storm with VLT/SINFONI. *Icarus*, *264*, 72–89. https://doi.org/10.1016/j.icarus.2015.09.010

315 Irwin, P. G. J., Teanby, N. A., Davis, G. R., Fletcher, L. N., Orton, G. S., Calcutt, S. B., …
316 Hurley, J. (2012). Further seasonal changes in Uranus' cloud structure observed by Gemini-
317 North and UKIRT. *Icarus*, *218*(1), 47–55. https://doi.org/10.1016/j.icarus.2011.12.001

318 Irwin, P. G. J., de Bergh, C., Courtin, R., Bézard, B., Teanby, N. A., Davis, G. R., Hurley, J.
319 (2012). The application of new methane line absorption data to Gemini-N/NIFS and
320 KPNO/FTS observations of Uranus' near-infrared spectrum. *Icarus*, *220*(2), 369–382.
321 https://doi.org/10.1016/j.icarus.2012.05.017

322 Irwin, P. G. J., Teanby, N. A., de Kok, R., Fletcher, L. N., Howett, C. J. A., Tsang, C. C. C., …
323 Parrish, P. D. (2008). The NEMESIS planetary atmosphere radiative transfer and retrieval
324 tool. *Journal of Quantitative Spectroscopy and Radiative Transfer*, *109*(6), 1136–1150.
325 https://doi.org/10.1016/j.jqsrt.2007.11.006

326 Irwin, P. G. J., Wong, M. H., Simon, A. A., Orton, G. S., & Toledo, D. (2017). HST/WFC3
327 observations of Uranus' 2014 storm clouds and comparison with VLT/SINFONI and
328 IRTF/Spex observations. *Icarus*, *288*, 99–119. https://doi.org/10.1016/j.icarus.2017.01.031

329 Karkoschka, E. (2001). Uranus' apparent seasonal variability in 25 HST filters. *Icarus*, *151*(1),
330 84–92. https://doi.org/10.1006/icar.2001.6599

331 Karkoschka, E., & Tomasko, M. (2009). The haze and methane distributions on Uranus from
332 HST-STIS spectroscopy. *Icarus*, *202*(1), 287–309.
333 https://doi.org/10.1016/J.ICARUS.2009.02.010

334 de Kleer, K., Luszcz-Cook, S., de Pater, I., Ádámkovics, M., & Hammel, H. B. (2015). Clouds
335 and aerosols on Uranus: Radiative transfer modeling of spatially-resolved near-infrared
336 Keck spectra. *Icarus*, *256*(Supplement C), 120–137.
337 https://doi.org/https://doi.org/10.1016/j.icarus.2015.04.021

338 Lockwood, G. W., & Jerzykiewicz, M. (2006). Photometric variability of Uranus and Neptune,
339 1950-2004. *Icarus*, *180*(2), 442–452. https://doi.org/10.1016/j.icarus.2005.09.009

340 de Pater, I., Sromovsky, L. A., Fry, P. M., Hammel, H. B., Baranec, C., & Sayanagi, K. M.
341 (2015). Record-breaking storm activity on Uranus in 2014. *Icarus*, *252*, 121–128.
342 https://doi.org/10.1016/j.icarus.2014.12.037

343 Pollack, J. B., K. Rages, S. K. Pope, M. G. Tomasko, P. N. Romani, and S. K. Atreya
344 (1987). Nature of the stratospheric haze on Uranus: Evidence for condensed
345 hydrocarbons. J. Geophys. Res., 92(A13), 15037–15065, doi:10.1029/JA092iA13p15037.

346 Rages, K. A., Hammel, H. B., & Friedson, A. J. (2004). Evidence for temporal change at Uranus'
347 south pole. *Icarus*, *172*(2), 548–554. https://doi.org/10.1016/j.icarus.2004.07.009

348 Sheik-Bahae, M., (2005). Nonlinear Optics Basics. KramersKronig Relations in Nonlinear
349 Optics. In Robert D. Guenther. Encyclopedia of Modern Optics. Amsterdam: Academic
350 Press.

351 Sromovsky, L. A., & Fry, P. M. (2007). Spatially resolved cloud structure on Uranus:
352 Implications of near-IR adaptive optics imaging. *Icarus*, *192*(2), 527–557.

https://doi.org/10.1016/j.icarus.2007.07.017

Sromovsky, L. A., Fry, P. M., & Kim, J. H. (2011). Methane on Uranus: The case for a compact CH_4 cloud layer at low latitudes and a severe CH_4 depletion at high-latitudes based on re-analysis of Voyager occultation measurements and STIS spectroscopy. *Icarus*, *215*(1), 292–312. https://doi.org/10.1016/j.icarus.2011.06.024

Sromovsky, L. A., de Pater, I., Fry, P. M., Hammel, H. B., & Marcus, P. (2015). High S/N Keck and Gemini AO imaging of Uranus during 2012-2014: New cloud patterns, increasing activity, and improved wind measurements. https://doi.org/10.1016/j.icarus.2015.05.029

Sromovsky, L. A., Karkoschka, E., Fry, P. M., Hammel, H. B., de Pater, I., & Rages, K. (2014). Methane depletion in both polar regions of Uranus inferred from HST/STIS and Keck/NIRC2 observations. *Icarus*, *238*, 137–155. https://doi.org/10.1016/j.icarus.2014.05.016

Tice, D. S., Irwin, P. G. J., Fletcher, L. N., Teanby, N. A., Hurley, J., Orton, G. S., & Davis, G. R. (2013). Uranus' cloud particle properties and latitudinal methane variation from IRTF SpeX observations. *Icarus*, *223*(2), 684–698. https://doi.org/10.1016/j.icarus.2013.01.006

Zheng, C., & Borysow, A. (1995). Modeling of collision-induced infrared absorption spectra of H_2 pairs in the first overtone band at temperatures from 20 to 500 K. *Icarus*, *113*(1), 84–90. https://doi.org/10.1006/icar.1995.1006